

# Bidirectional Dilation Transformer for Multispectral and Hyperspectral Image Fusion

Shangqi Deng<sup>1</sup>, Liang-Jian Deng<sup>2\*</sup>, Xiao Wu<sup>3</sup> and Ran Ran<sup>4</sup> and Rui Wen<sup>4</sup>

University of Electronic Science and Technology of China, Chengdu, 611731

shangqideng0124@gmail.com, liangjian.deng@uestc.edu.cn, wxwx1997@gmail.com, ranran@std.uestc.edu.cn, wenrui202102@163.com.

## Abstract

Transformer-based methods have proven to be effective in achieving long-distance modeling, capturing the spatial and spectral information, and exhibiting strong inductive bias in various computer vision tasks. Generally, the Transformer model includes two common modes of multi-head self-attention (MSA): spatial MSA (Spa-MSA) and spectral MSA (Spe-MSA). However, Spa-MSA is computationally efficient but limits the global spatial response within a local window. On the other hand, Spe-MSA can calculate channel self-attention to accommodate high-resolution images, but it disregards the crucial local information that is essential for low-level vision tasks. In this study, we propose a bidirectional dilation Transformer (BDT) for multispectral and hyperspectral image fusion (MHIF), which aims to leverage the advantages of both MSA and the latent multiscale information specific to MHIF tasks. The BDT consists of two designed modules: the dilation Spa-MSA (D-Spa), which dynamically expands the spatial receptive field through a given hollow strategy, and the grouped Spe-MSA (G-Spe), which extracts latent features within the feature map and learns local data behavior. Additionally, to fully exploit the multiscale information from both inputs with different spatial resolutions, we employ a bidirectional hierarchy strategy in the BDT, resulting in improved performance. Finally, extensive experiments on two commonly used datasets, CAVE and Harvard, demonstrate the superiority of BDT both visually and quantitatively. Furthermore, the related code is available at <https://github.com/Dengshangqi/BDT>.

## 1 Introduction

Hyperspectral imaging (HSI) is a widely used technology in various fields, including agriculture [Lu *et al.*, 2020;

\*Corresponding author: Liang-Jian Deng. This research is supported by NSFC (12271083) and Natural Science Foundation of Sichuan Province (2022NSFSC0501).

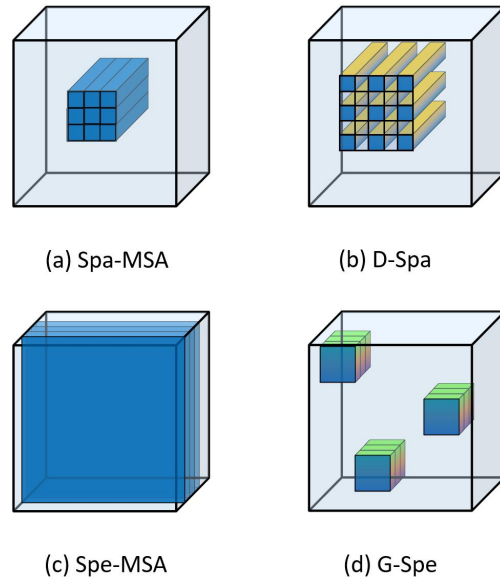


Figure 1: The comparison of (a) Spa-MSA [Liu *et al.*, 2021], (b) the proposed D-Spa based on Spa-MSA [Zamir *et al.*, 2022], and (d) the proposed G-Spe based on Spe-MSA. The blue clusters indicate the image tokens in (a) and (b). Utilizing the dilation operation, the proposed D-Spa can expand the receptive field of Spa-MSA. In (c) and (d), the blue slices denote the image tokens, and we design G-Spe to allow the model to learn more data behavior inside the feature map.

Wu *et al.*, 2011], food safety [Feng and Sun, 2012], biomedical diagnostics [Piqueras *et al.*, 2011], and atmospheric environment detection [Gao *et al.*, 2006]. HSIs with high spectral resolution produce precise spectral characteristic curves, and the abundance of bands makes it convenient for mutual band correction. However, due to the current physical imaging technology’s constraints, there is a trade-off between the spatial and spectral resolution of the natural imaging process. Therefore, it is impossible to produce an image with high spatial and spectral resolution simultaneously. As a result, multispectral and hyperspectral image fusion (MHIF) has emerged as a promising method to generate the necessary high-resolution hyperspectral images (HR-HSI). Numerous approaches have been developed for MHIF and can be broadly categorized into two categories: traditional methods [Guo *et al.*, 2020; Yang *et al.*, 2020b; Yang *et al.*, 2020a]

38  
39  
40  
41  
42  
43  
44  
45  
46  
47  
48  
49  
50  
51  
52  
53

54 and deep learning (DL)-based techniques [Yan *et al.*, 2022;  
55 Zhou *et al.*, 2022; Cao *et al.*, 2020].

56 In recent years, deep learning (DL)-based techniques have  
57 become increasingly popular, with CNN modules being  
58 the current state-of-the-art for MHIF problems due to their  
59 spatial-agnostic and channel-specific convolutional proper-  
60 ties [Li *et al.*, 2021]. Researchers have designed specific  
61 convolution modules and stacked them to construct a gen-  
62 eral network structure that effectively extracts potential be-  
63 havior from databases. However, the local receptive field in  
64 CNNs limits long-range dependencies and may hinder the in-  
65 ternal modeling of the image. Recently, the Vision Trans-  
66 former (ViT)[Kolesnikov *et al.*, 2021] has demonstrated im-  
67 pressive performance on various computer vision tasks[Hu  
68 *et al.*, 2022]. ViT is based on a self-attention mechanism that  
69 efficiently captures global interactions by studying the con-  
70 nections among tokens. To apply the Transformer to visual  
71 tasks, numerous solutions have emerged, such as the spa-  
72 tial window-based MSA [Liu *et al.*, 2021], Spe-MSA [Za-  
73 mir *et al.*, 2022], linear complexity self-attention [Wang  
74 *et al.*, 2020], among others. Notably, the spatial window-based  
75 MSA sets a suitable window size and divides the spatial size  
76 of an image into several patches. For concision, this method  
77 is also referred to as Spa-MSA.

78 We propose a fusion architecture that integrates spatial and  
79 spectral information and fully exploits MSA to model simi-  
80 lar patches in a hyperspectral image, considering the proper-  
81 ties of the MHIF task. While Spa-MSA lacks the modeling  
82 of longer-distance information, Spe-MSA does not make full  
83 use of the information inside the data. To achieve a more  
84 wide-range correlation, our proposed architecture includes  
85 dilation Spa-MSA and grouped Spe-MSA modules. The con-  
86 tributions of this paper are listed as follows (also find more  
87 details in Fig. 1):

- 88 • We present a novel bidirectional dilation Transformer  
89 (BDT) architecture that utilizes both dilation Spa-MSA  
90 (D-Spa) and grouped Spe-MSA (G-Spe) modules for  
91 MHIF. Our experimental results on benchmark datasets  
92 demonstrate that our method achieves state-of-the-art  
93 (SOTA) performance. We also conduct additional ex-  
94 periments to evaluate the efficiency of D-Spa and G-Spe  
95 modules, the bidirectional structures, and the impact of  
96 dilation rates on the overall performance.
- 97 • To improve the receptive field of Spa-MSA, we design  
98 the D-Spa to extract a broader range of local informa-  
99 tion for the MHIF task. Specifically, D-Spa does not  
100 require additional parameters and calculations, which  
101 can be viewed as a plug-and-play module for all Spa-  
102 MSA based approaches. Various experiments in Sect. 3  
103 demonstrate the effectiveness of the proposed dilation  
104 strategy.
- 105 • To fully exploit the spatial information along channel di-  
106 mension, we design a so-called G-Spe to extract latent  
107 features inside the feature map and learn local data be-  
108 havior.

## 109 2 Related Works

### 2.1 Transformer in MHIF

110 The Transformer architecture has demonstrated strong per-  
111 formance in various vision tasks, and many researchers are  
112 attempting to leverage it for the MHIF problem with promis-  
113 ing results. For instance, Hu *et al.*[Hu *et al.*, 2022] were  
114 the first to use Transformer for MHIF and achieved power-  
115 ful performance with a lightweight network. Addition-  
116 ally, Meng *et al.*[Meng *et al.*, 2022] proposed an advanced  
117 transformer-based model for remote sensing pansharpening.  
118 Bandara *et al.*[Bandara and Patel, 2022] designed a novel  
119 attention mechanism for hyperspectral pansharpening using  
120 Transformer, where the features of the low-resolution hy-  
121 perspectral image (LR-HSI) and panchromatic (PAN) im-  
122 age were formulated as queries and keys. Ma *et al.*[Ma  
123 *et al.*, 2021] utilized Transformer instead of CNN to learn the  
124 prior of hyperspectral images (HSIs) and then used an un-  
125 folding network to simulate iterative solution processes for  
126 HSI super-resolution. Furthermore, Zhou *et al.* [Zhou  
127 *et al.*, 2021] proposed a customized Transformer that facilitates col-  
128 laborative feature learning across two modalities for remote  
129 sensing pansharpening.  
130

### 2.2 Motivation

131 Despite the promising outcomes of the aforementioned meth-  
132 ods, which largely rely on the powerful self-attention mod-  
133 ule, they often adopt the self-attention or Transformer struc-  
134 ture for various image fusion tasks without fully considering  
135 their deficiencies, especially for the specific MHIF problem.  
136 For instance, Spa-MSA can restore image details and reduce  
137 computational complexity by correlating local pixels, but its  
138 receptive field is significantly restricted by the window size.  
139 Similarly, previous Spe-MSA treats channels as tokens and  
140 uses the information of the entire space for self-attention, but  
141 this does not fully utilize the information inside the image.  
142 To address the issue of Spa-MSA, we are inspired by the con-  
143 cept of dilation convolution [Li *et al.*, 2018b] to design a new  
144 2D dilation structure specifically for Spa-MSA called D-Spa.  
145 D-Spa can effectively enlarge the receptive field without in-  
146 troducing additional parameters or computational complex-  
147 ity. To address the issue of Spe-MSA, we propose a Grouped  
148 G-Spe that groups the space and then performs Spe-MSA in  
149 small groups, which may extract information within the fea-  
150 ture and better learn local data behavior. Additionally, we  
151 design a bidirectional hierarchy structure for better exploiting  
152 multiscale information of the two inputs, which have different  
153 spatial resolutions, for the specific application of MHIF.  
154

## 3 Methodology

155 In this section, we present our BDT designed for the MHIF  
156 task. We first introduce the overall architecture of our BDT in  
157 Sec. 3.1. Subsequently, we analyse the function of D-Spa in  
158 Sec. 3.2. Finally, we describe the design of G-Spe in Sec. 3.3.  
159

### 3.1 The Overall Architecture

160 Our BDT is outlined in Fig. 2, which is a hierarchical bidirec-  
161 tional input architecture with two stages, *i.e.*, Bimodal Fea-  
162 ture Extraction (BFE) and Bimodal Feature Fusion (BFF).  
163 In order to extract spatial information, we concatenate the  
164

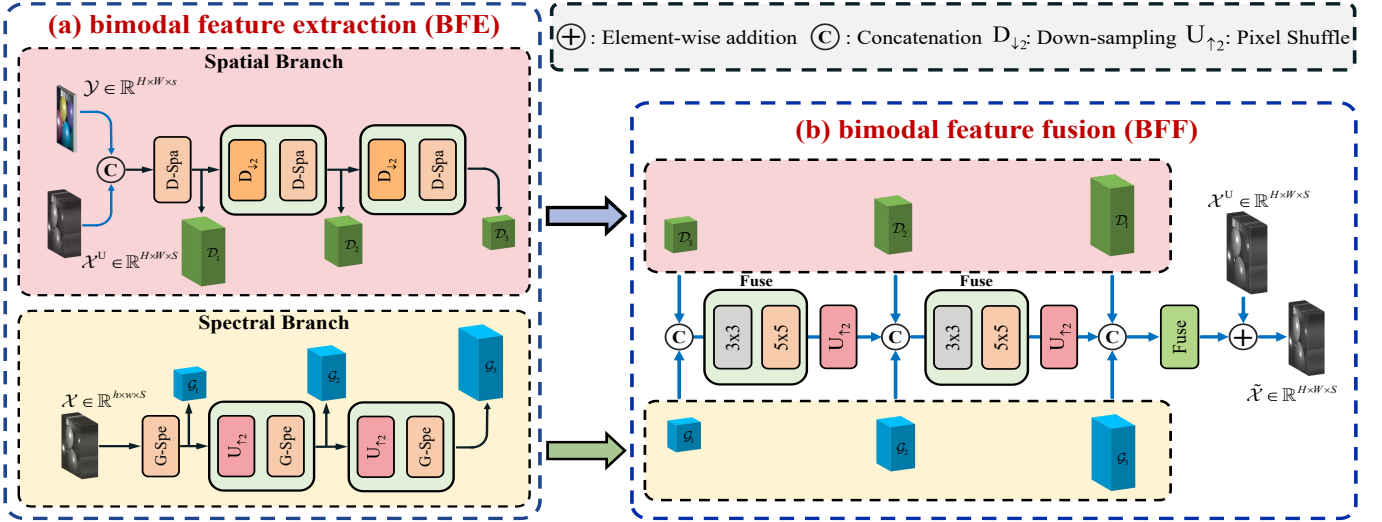


Figure 2: The overall architecture of the proposed BDT approach. (a) The diagram of proposed BFE consisted of spatial and spectral branches. (b) The inputs of proposed BFF are the output of the spectral branch and the spatial branch in the BFE, respectively. Please note that  $\mathcal{X}$  is the LR-HSI,  $\mathcal{Y}$  is the HR-MSI and  $\mathcal{X}^U$  is the bicubic interpolation LR-HSI.  $\mathcal{D}_i$  and  $\mathcal{G}_i$  respectively represent spatial information and spectral information extracted from bimodal feature extraction (BFE), *i.e.*, the subgraph on the left. Then,  $\mathcal{D}_i$  and  $\mathcal{G}_i$  are paired into the bimodal feature fusion (BFF) to generate the final output, *i.e.*, the subgraph on the right.

165 bicubic interpolated LR-HSI  $\mathcal{X}^U \in \mathbb{R}^{H \times W \times S}$  and HR-MSI  
 166  $\mathcal{Y} \in \mathbb{R}^{H \times W \times s}$  as the input of the spatial branch. Besides, D-  
 167 Spa in BFE is designed to learn the spatial information, where  
 168 output feature maps are  $\mathcal{D}_i$ ,  $i = 1, 2, 3$ . In detail, the process  
 169 of BFE is as follows:

$$\mathcal{D}_i = \text{SpatialBranch}(\text{Conv}_1(\text{Cat}(\mathcal{Y}, \mathcal{X}^U))), \quad (1)$$

170 where  $\text{Conv}_1$  is a convolutional structure. Using HR-HSI  
 171  $\mathcal{X} \in \mathbb{R}^{h \times w \times S}$  as the input of the spectral branch, the in-  
 172 formation on the spectrum is dynamically learned through G-  
 173 Spe, and outputs feature maps  $\mathcal{G}_i$  ( $i = 1, 2, 3$ ) as shown in the  
 174 following formula:

$$\mathcal{G}_i = \text{SpectralBranch}(\text{Conv}_2(\mathcal{X})), \quad (2)$$

175 where  $\text{Conv}_2$  is a multi-layer convolution structure used to in-  
 176 crease the channels. To fuse the feature maps, *i.e.*,  $\mathcal{D}_i$  and  $\mathcal{G}_i$ ,  
 177 we design the BFF model, which is an efficient two-layer con-  
 178 volutional structure. In detail, we concatenate  $\mathcal{D}_3$  and  $\mathcal{G}_1$  first,  
 179 and send the concatenated one to the fusion module which in-  
 180 volves a  $3 \times 3$  kernel and a  $5 \times 5$  kernel, and then upsample  
 181 through PixelShuffle, as shown in the following formula:

$$\mathcal{F}_1 = \text{PixelShuffle}(\text{Fuse}(\text{Cat}(\mathcal{D}_3, \mathcal{G}_1))). \quad (3)$$

182 Then, we concatenate  $\mathcal{F}_1$ ,  $\mathcal{D}_2$  and  $\mathcal{G}_2$  together, and upsample  
 183 the concatenated result. After that, we fuse the upsampled  
 184 result as the following formula:

$$\mathcal{F}_2 = \text{PixelShuffle}(\text{Fuse}(\text{Cat}(\mathcal{F}_1, \mathcal{D}_2, \mathcal{G}_2))). \quad (4)$$

185 Finally, we add the fusion results of  $\mathcal{F}_2$ ,  $\mathcal{D}_3$  and  $\mathcal{G}_1$  to the  
 186 Bicubic interpolated LR-HSI  $\mathcal{X}^U$ , and the final output  $\tilde{\mathcal{X}} \in$   
 187  $\mathbb{R}^{H \times W \times S}$  is expressed by the following formula:

$$\tilde{\mathcal{X}} = \text{Fuse}(\text{Cat}(\mathcal{F}_2, \mathcal{D}_3, \mathcal{G}_1)) + \mathcal{X}^U. \quad (5)$$

### 3.2 D-Spa

188 Vanilla convolution is a fundamental building block of  
 189 convolutional neural networks (CNNs) which have seen  
 190 tremendous success in several computer vision tasks, *e.g.*,  
 191 image classification [Hong *et al.*, 2021], image super-  
 192 resolution [Liang *et al.*, 2021], and image segmentation [Liu  
 193 *et al.*, 2021]. Dilation convolution increases the receptive  
 194 field of the convolution kernel without adding additional pa-  
 195 rameters, retains the internal structure of data and avoids us-  
 196 ing a pooling layer to downsample the feature map. The di-  
 197 lation convolution operation with elements  $k \times k$  in the ker-  
 198 nel and a dilation rate  $d$  at the  $(i, j)$ th pixel position can be  
 199 expressed as a linear combination of input  $\mathbf{F} \in \mathbb{R}^{C \times H \times W}$   
 200 around  $(i, j)$ th pixel position, which can be expressed as fol-  
 201 lows:  
 202

$$\mathbf{F}'_{(:,i,j)} = \sum_{(x,y) \in \Omega(i,j)} \mathbf{W}[\mathbf{P}_{(i,j)} - \mathbf{P}_{(x,y)}] \mathbf{F}_{(:,x,y)}, \quad (6)$$

203 where  $\mathbf{F}_{(:,x,y)} \in \mathbb{R}^C$  indicates the vector of the  $(x, y)$ th pixel  
 204 position in the input feature map  $\mathbf{F}$ ;  $\Omega(i, j)$  represents the co-  
 205 ordinate set of the dilation area centered on the  $(i, j)$ th pixel  
 206 position;  $\mathbf{F}'_{(:,i,j)} \in \mathbb{R}^{C'}$  indicates the vector of the  $(i, j)$ th  
 207 pixel position in the output feature map  $\mathbf{F}' \in \mathbb{R}^{C' \times H \times W}$  and  
 208  $\mathbf{W} \in \mathbb{R}^{C' \times C \times k \times k}$  is the convolution kernel of  $k \times k$ , where  
 209  $\mathbf{W}[\mathbf{P}_{(i,j)} - \mathbf{P}_{(x,y)}] \in \mathbb{R}^{C' \times C}$  means the convolution kernel  
 210 weight which contains coordinate offset  $[\mathbf{P}_{(i,j)} - \mathbf{P}_{(x,y)}] \in$   
 211  $\{(-\frac{k+1}{2}d, -\frac{k+1}{2}d), (-\frac{k-1}{2}d, -\frac{k-1}{2}d), \dots, (\frac{k-1}{2}d, \frac{k-1}{2}d)\}$   
 212 with dilation rate  $d$ . Jiao *et al.* [Jiao *et al.*, 2023] used the  
 213 unfold operation to implement the expansion of the window  
 214 and designed a sliding mode. However, our D-Spa expands  
 215 the window in fixed position, instead of sliding it pixel by  
 216 pixel, and expands windows by index values. Han *et al.* [Han

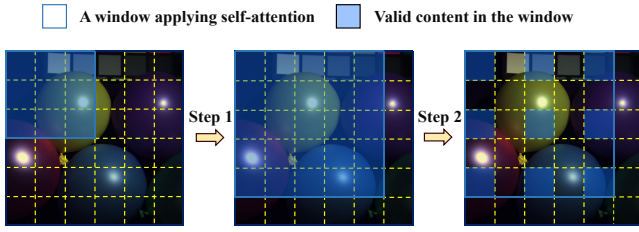


Figure 3: The dilation in D-Spa (dilation rate = 2) consists of two steps, *i.e.*, expanding and hollowing. Step 1 expands the  $3 \times 3$  window to  $5 \times 5$ , and step 2 hollows out part of the window.

*et al.*, 2021] present a novel point of view, which regards Spa-MSA as a variant of convolution, with the properties of sparse connectivity, weight sharing, depth separation, and dynamic weight. To this end, we can represent D-Spa in the form of convolution.

We operate three  $1 \times 1$  convolutions on the input feature  $\mathbf{F} \in \mathbb{R}^{C \times H \times W}$  to generate three tensors, *i.e.*,  $\mathbf{Q} \in \mathbb{R}^{C \times H \times W}$ ,  $\mathbf{K} \in \mathbb{R}^{C \times H \times W}$  and  $\mathbf{V} \in \mathbb{R}^{C \times H \times W}$ , respectively. Taking only one head in D-Spa as an example, given a window size  $k$  and a dilation rate  $d$  of 2, the output  $\mathbf{V}' \in \mathbb{R}^{C \times H \times W}$  of D-Spa operation at the  $(i, j)$ th pixel position can be expressed as a linear aggregation of corresponding values  $\mathbf{V} \in \mathbb{R}^{C \times H \times W}$  in the local window containing the  $(i, j)$ th pixel position.

$$\mathbf{V}'_{(:,i,j)} = \sum_{(x,y) \in \Omega(i,j)} \mathbf{W}_{(i,j \rightarrow x,y)} \mathbf{V}_{(:,x,y)}, \quad (7)$$

where  $\mathbf{V}_{(:,x,y)} \in \mathbb{R}^C$  indicates the value of the  $(x, y)$ th pixel position in the values map  $\mathbf{V} \in \mathbb{R}^{C \times H \times W}$ ;  $\Omega(i, j)$  indicates the coordinate set of a dilation window which contains  $k \times k$  pixel positions. In Fig. 3, the solid blue box represents the window applied self-attention. Taking the window size of  $3 \times 3$  and dilation rate of 2 as an example, the window shape becomes  $5 \times 5$  after dilating, and the blue patches in the window indicate the tokens that validly participates in the self-attention computation. The area  $\Omega(i, j)$  is generated by two steps, *i.e.*, the first step is to expand the original window, and the second is to prohibit some tokens from participating in the calculation of Spa-MSA. In Eq. 7,  $D$  is a constant variable;  $\mathbf{V}'_{(:,i,j)} \in \mathbb{R}^C$  indicates the vector of the  $(i, j)$ th pixel position in the output feature map  $\mathbf{V}' \in \mathbb{R}^{C \times H \times W}$ ;  $\mathbf{W}_{(i,j \rightarrow x,y)} \in \mathbb{R}$  indicates an element in the attention matrix which is computed as the softmax normalization of the dot-product between the query  $\mathbf{Q}_{(i,j)} \in \mathbb{R}^C$  and the key  $\mathbf{K}_{(x,y)} \in \mathbb{R}^C$ :

$$\mathbf{W}_{(i,j \rightarrow x,y)} = \frac{e^{\frac{1}{\sqrt{D}} \mathbf{Q}_{(i,j)}^T \mathbf{K}_{(x,y)}}}{S_i}, \quad (8)$$

where

$$S_i = \sum_{x=1, y=1}^{k,k} e^{\frac{1}{\sqrt{D}} \mathbf{Q}_{(i,j)}^T \mathbf{K}_{(x,y)}}. \quad (9)$$

By observing the generation of  $\mathbf{W} \in \mathbb{R}^{k \times k}$  in the Eq. 8, the D-Spa is a convolution operation with the content-aware characteristic. In other words, it dynamically generates weights

at each position. Fig. 1 above shows the properties of Spa-MSA and D-Spa. It can find that D-Spa can expand receptive fields like dilation convolution and learn the local information simultaneously. Furthermore, the D-Spa is pre-fixed, has no sliding characteristic, and adopts a multi-head attention mechanism, which groups the channels first, and each group shares a learned parameter.

### 3.3 G-Spe

Fully connected layer (FC) [Gardner and Dorling, 1998] is a basic linear unit in the CNNs, which connects the two hidden layers with the learnable parameters. Given input is  $\mathbf{F} \in \mathbb{R}^{HW \times C}$ , and the parameters of FC can be expressed as a matrix  $\mathbf{W} \in \mathbb{R}^{C \times C'}$ , the FC can be expressed in the form of matrix multiplication:

$$\mathbf{F}' = \mathbf{F} \mathbf{W}, \quad (10)$$

where  $\mathbf{F}' \in \mathbb{R}^{HW \times C'}$  is the output of FC, and  $\mathbf{W}$  is updated by the backpropagating gradient. However, the weight of FC is as spatial-agnostic as the vanilla convolution kernel, which does not build a relationship with the input. In order to better express the channel-wise relationship with the input, Hu *et al.* [Hu *et al.*, 2018] propose the idea of channel-attention (CA), which can be represented by:

$$\mathbf{F}' = \mathbf{F} \odot \mathbf{W}, \quad (11)$$

where  $\mathbf{F}' \in \mathbb{R}^{HW \times C}$  is the output of CA,  $\odot$  represents dot product operation and  $\mathbf{W} \in \mathbb{R}^C$  is learned from the following formula:

$$\mathbf{W} = \Phi(\mathbf{F}), \quad (12)$$

where  $\mathbf{W}$  is a weight learned by the network  $\Phi$  from the input  $\mathbf{F}$ , whose value is content-aware with the input. From this view, the weights in Spe-MSA are also content-aware, *i.e.*, Spe-MSA generates a weight matrix using spatial similarity.

In the Spe-MSA, the weight contains spatially related information, and the matrix multiplication operation can be regarded as a dynamic FC operation on one head of Spe-MSA. Given the Spe-MSA with one head, the process can be demonstrated as follows:

$$\mathbf{V}' = \mathbf{V} \mathbf{W}, \quad (13)$$

where  $\mathbf{V}' \in \mathbb{R}^{HW \times C}$  indicates the output of Spe-MSA,  $\mathbf{V} \in \mathbb{R}^{HW \times C}$  means the value of Spe-MSA, and  $\mathbf{W} \in \mathbb{R}^{C \times C}$  is generated by the following formula:

$$\mathbf{W}_{(i,j)} = \frac{e^{\frac{1}{\sqrt{D}} (\mathbf{K}_{(:,i)})^T \mathbf{Q}_{(i,j)}}}{S_j}, \quad (14)$$

in which

$$S_j = \sum_{i=1}^C e^{\frac{1}{\sqrt{D}} (\mathbf{K}_{(:,i)})^T \mathbf{Q}_{(i,j)}}}, \quad (15)$$

where  $\mathbf{Q} \in \mathbb{R}^{HW \times C}$  means the query of input;  $\mathbf{K} \in \mathbb{R}^{HW \times C}$  means the key of input;  $\mathbf{W}_{(i,j)}$  indicates the  $(i, j)$ th position of weight matrix  $\mathbf{W} \in \mathbb{R}^{C \times C}$ , which is generated by softmax normalization of the dot product between query

294  $\mathbf{Q}_{(:,j)} \in \mathbb{R}^{HW}$  and key  $\mathbf{K}_{(:,i)} \in \mathbb{R}^{HW}$ ;  $S_j$  is the result of  
 295 summing the  $j$ th column in the matrix generated by the num-  
 296 erator in Eq. 14 and  $D$  is a constant variable. By comparing  
 297 the weight generation in Eq. 10, Eq. 11, and Eq. 13, we can  
 298 find that Spe-MSA has the dense connection properties of FC  
 299 and the content-aware ability of CA, which means that Spe-  
 300 MSA dynamically establishes the connection between chan-  
 301 nels. To make full use of high-resolution spatial information  
 302 and local content in HR-MSI, we envisage the G-Spe as a  
 303 grouped design for space. In detail, we subdivide the value  
 304  $\mathbf{V} \in \mathbb{R}^{HW \times C}$ ,  $\mathbf{Q} \in \mathbb{R}^{HW \times C}$ , and  $\mathbf{K} \in \mathbb{R}^{HW \times C}$  into  
 305  $g^2$  groups, and in the  $k$ th group we get the corresponding  
 306  $\mathbf{V}^k \in \mathbb{R}^{\frac{HW}{g^2} \times C}$ ,  $\mathbf{Q}^k \in \mathbb{R}^{\frac{HW}{g^2} \times C}$  and  $\mathbf{K}^k \in \mathbb{R}^{\frac{HW}{g^2} \times C}$ , where  
 307  $k \in \{1, 2, 3, \dots, \frac{HW}{g^2}\}$ . Then we calculate the weight ma-  
 308 trix  $\mathbf{W}^k \in \mathbb{R}^{C \times C}$  in the  $k$ th group independently as follows:  
 309

$$\mathbf{W}_{(i,j)}^k = \frac{e^{\frac{1}{\sqrt{D}}(\mathbf{K}_{(:,i)}^k)^T \mathbf{Q}_{(:,j)}^k}}{S_j^k}, \quad (16)$$

310 where the  $S_j^k$  is calculated by the following formula:

$$S_j^k = \sum_{i=1}^C e^{\frac{1}{\sqrt{D}}(\mathbf{K}_{(:,i)}^k)^T \mathbf{Q}_{(:,j)}^k}. \quad (17)$$

311 We will perform matrix multiplication between  $\mathbf{W}^k$  and  $\mathbf{V}^k$ ,  
 312 as shown in the following formula:

$$\mathbf{V}^{k'} = \mathbf{V}^k \mathbf{W}^k. \quad (18)$$

313 Each group of G-Spe realizes a kind of dynamic FC oper-  
 314 ation, *i.e.*, a content-aware weight generator. We merge  
 315 together the calculated  $\mathbf{V}^{k'} \in \mathbb{R}^{\frac{HW}{g^2} \times C}$  according to the  
 316 spatial dimension to get the output  $\mathbf{V}' \in \mathbb{R}^{HW \times C}$ , where  
 317  $k \in \{1, 2, 3, \dots, \frac{HW}{g^2}\}$ . In this way, G-Spe realizes the  
 318 grouped design along the spatial dimension through the regu-  
 319 lar space subdivision so that the model has a rich information  
 320 expression capability. In Fig. 1 above, we describe the rela-  
 321 tionship between Spe-MSA and G-Spe. It can be found that  
 322 the Spe-MSA uses the characteristics of the entire space to  
 323 obtain weights, while G-Spe uses part of the spatial informa-  
 324 tion to get dynamic weights. Due to the property of the MHIF  
 325 task, local rich representations have certain advantages, and  
 326 the effect of G-Spe is better than Spe-MSA. Furthermore, we  
 327 design various experiments in Sec. 3 to verify this statement.

328 **Overall Loss Function:** We optimize the parameters of the  
 329 network in a unified and end-to-end manner. The overall loss  
 330 function consists of the weighted sum of two losses:

$$\mathcal{L}_{total} = \mathcal{L}_1 + \lambda_{ssim} \mathcal{L}_{ssim}, \quad (19)$$

331 where  $\mathcal{L}_1$  means Sum of Absolute Difference, the loss  $\mathcal{L}_{ssim}$   
 332 is expressed as:

$$\mathcal{L}_{ssim} = 1 - \text{SSIM}(\bar{\mathcal{X}}, \tilde{\mathcal{X}}), \quad (20)$$

333 where the SSIM<sup>1</sup> means Structural SIMilarity,  $\bar{\mathcal{X}}$  represents  
 334 the reference,  $\tilde{\mathcal{X}}$  denotes the output of our network, and  $\lambda_{ssim}$   
 335 is a positive hyperparameter fixed to 0.1 in our experiments.

<sup>1</sup>[https://en.wikipedia.org/wiki/Structural\\_similarity](https://en.wikipedia.org/wiki/Structural_similarity)

## 4 Experiments

**Datasets:** To test the performance of our model, we conduct  
 experiments on the CAVE<sup>2</sup> and Harvard<sup>3</sup> datasets. CAVE  
 dataset contains 32 HSIs, including 31 spectral bands rang-  
 ing from 400 nm to 700 nm at 10 nm steps. We randomly  
 select 20 images for training the network, and the remaining  
 11 images constitute the testing dataset. In addition, Harvard  
 dataset contains 77 HSIs of indoor and outdoor scenes, and  
 each HSI has a size of  $1392 \times 1040 \times 31$ , covering the spec-  
 tral range from 420 nm to 720 nm. We crop the upper left  
 part ( $1000 \times 1000$ ) of the 20 Harvard images, 10 of which  
 have been used for training, and the rest has been exploited  
 for testing.

**Data Simulation:** The proposed network takes LR-HSI and  
 HR-MSI ( $\mathcal{X}, \mathcal{Y}$ ) as input pairs, while the ground-truth (GT)  
 for training is HR-HSI  $\bar{\mathcal{X}}$ . However, since HR-HSI is not  
 available as a reference, a simulation stage is required. In our  
 experiments using the CAVE dataset, we produce 3920 over-  
 lapping patches with a size of  $64 \times 64 \times 31$  by cropping 20  
 chosen training images. These patches serve as the HR-HSI  
 (ground-truth)  $\bar{\mathcal{X}}$  patches. To simulate appropriate LR-HSIs,  
 we apply a  $3 \times 3$  Gaussian blur kernel with a standard devi-  
 ation of 0.5 to the original HR-HSIs. We then downsample  
 the blurred patches with a scaling factor of 4. The HR-MSI  
 patches are generated using the common spectral response  
 function of the Nikon D700<sup>4</sup> camera. Therefore, the input  
 pairs ( $\mathcal{X}, \mathcal{Y}$ ) consist of 3920 LR-HSI patches with a size of  
 $16 \times 16 \times 31$  and RGB image patches with a size of  $64 \times 64 \times 3$ .  
 The pairs and their related GTs are randomly divided into  
 training data (80%) and validation data (20%). The same  
 procedure is used to simulate the input LR-HSI and HR-MSI  
 products and GTs for the Harvard dataset.

**Benchmark:** To assess the performance of our approach, we  
 compare it with various state-of-the-art methods for MHIF.  
 The upsampled LR-HSI in Fig. 2 is the bicubic-interpolated  
 result, which is added to the experiment as a baseline. Model-  
 based techniques include the MTF-GLP-HS [Selva *et al.*,  
 2015], the CSTF-FUS [Li *et al.*, 2018a], the LTTR [Dian  
*et al.*, 2019], the LTMR [Dian and Li, 2019], and the IR-  
 TenSR [Xu *et al.*, 2022] approaches. In addition, we perform  
 a comparison with other deep learning methods, such as the  
 DBIN [Wang *et al.*, 2019], the SSRNet [Zhang *et al.*, 2020],  
 the ResTFNet [Liu *et al.*, 2020], the HSRNet [Hu *et al.*,  
 2021], the MoG-DCN [Dong *et al.*, 2021], the Fusformer [Hu  
*et al.*, 2022] and the DHIF [Huang *et al.*, 2022] network. All  
 the deep learning approaches are trained with the same input  
 pairs for a fair comparison. Moreover, the related hyperpa-  
 rameters are selected consistent with the original papers.

**Implementation Details:** The proposed network implements  
 in PyTorch 1.11.0 and Python 3.7.0 using AdamW opti-  
 mizer with a learning rate of 0.0001 to minimize  $\mathcal{L}_{total}$  by  
 2000 epochs and Linux operating system with a NVIDIA  
 RTX3090 GPU.

**Results on CAVE Dataset:** We test our model on the CAVE  
 dataset. Fig. 4 presents the 11 testing images in an RGB

<sup>2</sup><https://www.cs.columbia.edu/CAVE/databases/multispectral/>

<sup>3</sup><http://vision.seas.harvard.edu/hyperspec/index.html>

<sup>4</sup>[https://www.maxmax.com/nikon\\_d700\\_study.htm](https://www.maxmax.com/nikon_d700_study.htm)

Table 1: Average quantitative comparisons on 11 CAVE examples and 10 Harvard examples simulating a scaling factor of 4. The best values are highlighted in bold, and the second best values are underlined. M refers to millions.

Methods	CAVE					Harvard				
	PSNR	SAM	ERGAS	SSIM	#params	PSNR	SAM	ERGAS	SSIM	#params
Bicubic	34.33±3.88	4.45±1.62	7.21±4.90	0.944±0.0291	-	38.71±4.33	2.53±0.67	4.45±41.81	0.948±0.0268	-
MTF-GLP-HS [Selva <i>et al.</i> , 2015]	37.69±3.85	5.33±1.91	4.57±2.66	0.973±0.0158	-	33.81±3.50	6.25±2.42	3.47±1.82	0.952±0.0321	-
CSTF-FUS [Li <i>et al.</i> , 2018a]	34.46±4.28	14.37±5.30	8.29±5.29	0.866±0.0747	-	39.13±3.50	6.91±2.66	4.64±1.80	0.913±0.0487	-
LTTR[Dian <i>et al.</i> , 2019]	35.85±3.49	6.99±2.55	5.99±2.92	0.956±0.0288	-	37.91±3.58	5.35±1.94	2.44±1.06	0.972±0.0183	-
LTMR[Dian and Li, 2019]	36.54±3.30	6.71±2.19	5.39±2.53	0.963±0.0208	-	38.41±3.58	5.05±1.70	2.24±0.97	0.970±0.0166	-
IR-TenSR[Xu <i>et al.</i> , 2022]	35.61±3.45	12.30±4.68	5.90±3.05	0.945±0.0267	-	40.47±3.04	4.36±1.52	5.57±1.57	0.962±0.0140	-
DBIN [Wang <i>et al.</i> , 2019]	50.83±4.29	2.21±0.63	1.24±1.06	0.996±0.0026	0.469M	47.88±3.87	2.31±0.46	1.95±0.81	0.988±0.0066	0.469M
ResTFNet [Liu <i>et al.</i> , 2020]	45.58±5.47	2.82±0.70	2.36±2.59	0.993±0.0056	2.387M	45.93±4.35	2.61±0.69	2.56±1.32	0.985±0.0082	2.387M
SSRNet [Zhang <i>et al.</i> , 2020]	48.62±3.92	2.54±0.84	1.63±1.21	0.995±0.0023	<b>0.027M</b>	47.95±3.37	2.31±0.60	2.30±1.42	0.987±0.0070	<b>0.027M</b>
HSRNet [Hu <i>et al.</i> , 2021]	50.38±3.38	2.23±0.66	1.20±0.75	0.996±0.0014	0.633M	48.29±3.03	2.26±0.56	1.87±0.81	0.988±0.0064	0.633M
MoG-DCN [Dong <i>et al.</i> , 2021]	51.63±4.10	2.03±0.62	1.11±0.82	0.997±0.0018	6.840M	47.89±4.09	2.11±0.52	1.89±0.82	0.988±0.0073	6.840M
Fusformer [Hu <i>et al.</i> , 2022]	49.98±8.10	2.20±0.85	2.50±5.21	0.994±0.0111	0.504M	47.87±5.13	2.84±2.07	2.04±0.99	0.986±0.0101	0.467M
DHIF [Huang <i>et al.</i> , 2022]	51.07±4.17	2.01±0.63	1.22±0.97	0.997±0.0016	22.462M	47.68±3.85	2.32±0.53	1.95±0.92	0.988±0.0074	22.462M
BDT (ours)	<b>52.30±3.98</b>	<b>1.93±0.55</b>	<b>1.02±0.77</b>	<b>0.997±0.0014</b>	2.668 M	<b>48.83±3.45</b>	<b>2.07±0.49</b>	<b>1.83±0.81</b>	<b>0.989±0.0067</b>	2.668 M
Ideal value	∞	0	0	1	-	∞	0	0	1	-

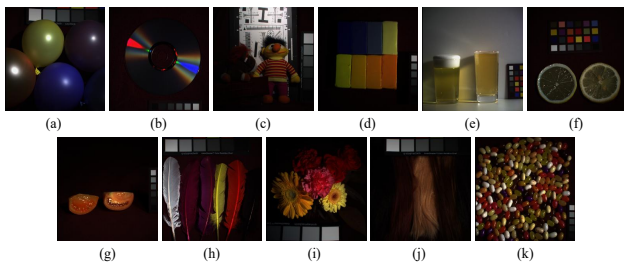


Figure 4: The testing images from the CAVE dataset: (a) balloons, (b) cd, (c) chart and stuffed toy, (d) clay, (e) fake and real beers, (f) fake and real lemon slices, (g) fake and real tomatoes, (h) feathers, (i) flowers, (j) hairs, and (k) jelly beans. An RGB color representation is used to depict the images.

## 4.1 Ablation Study

In this section, we provide an in-depth discussion of D-Spa and G-Spe in the BDT to demonstrate their effectiveness and rationale. We compare their performance with ablation on self-structure and other existing networks. To maintain generality and conciseness, we present our analysis based on the CAVE dataset.

Table 2: The average four QIs and the corresponding parameters on the CAVE dataset simulating a scaling factor of 4.

D-Spa	G-Spe	PSNR	SAM	ERGAS	SSIM
✓	✓	<b>52.30±3.98</b>	<b>1.93±0.55</b>	<b>1.02±0.77</b>	<b>0.997±0.0014</b>
✓	✗	52.03±3.79	2.02±0.59	1.04±0.75	0.997±0.0014
✗	✓	51.96±3.72	2.03±0.59	1.04±0.74	0.997±0.0013
✗	✗	51.91±3.77	2.02±0.59	1.05±0.76	0.997±0.0014

1) *D-Spa and G-Spe*: To verify the effectiveness, in Tab. 2, results show that replacing D-Spa with Spa-MSA will bring the performance gain, and replacing G-Spe with Spe-MSA will also boost performance. And our BDT utilizes both D-Spa and G-Spe obtaining the best results. It proves that the designed modules boost performance of networks. Please note that Spa-MSA and Spe-MSA indicates the dilation 1 of D-Spa and the group 1 of G-Spe in BDT, respectively.

Table 3: The average four QIs and the corresponding parameters on the CAVE dataset simulating a scaling factor of 4.

Methods	PSNR	SAM	ERGAS	SSIM
Swin-Shift	51.47 ± 3.88	2.08 ± 0.60	1.09 ± 0.81	0.997 ± 0.0015
Swin-D	<b>51.57 ± 4.00</b>	<b>2.04 ± 0.58</b>	<b>1.10 ± 0.85</b>	<b>0.997 ± 0.0016</b>
Restormer-T	50.67 ± 4.36	2.34 ± 0.72	1.29 ± 1.06	0.996 ± 0.0024
Restormer-G	<b>51.16 ± 3.93</b>	<b>2.22 ± 0.67</b>	<b>1.15 ± 0.79</b>	<b>0.996 ± 0.0017</b>

2) *Embedding in existing networks*: We test D-Spa against the Shifted Window operation in Swin Transformer and G-Spe against the Spe-MSA in Restormer. We use a Swin Transformer structure comparing the Shifted Window approach (Swin-Shift) with our D-Spa (Swin-D). And we also compare Restormer network structure with the transpose MSA (T-MSA) approach (Restormer-T) and our G-Spe

391 color composition. From Tab. 1, we can see that the proposed  
392 approach overcomes the other methods in 4 quality indexes  
393 (QIs), *i.e.*, PSNR, SAM, ERGAS, and SSIM. Specifically,  
394 we observe an improvement of  $\sim 1.30/4.93/8.11/0.028\%$   
395 in PSNR/SAM/ERGAS/SSIM compared to the second best  
396 method, *i.e.*, MoG-DCN [Dong *et al.*, 2021]. Com-  
397 pared with the third best method, DHIF [Huang *et al.*,  
398 2022], our approach gets the gains  $\sim 2.41/3.98/16/0.09\%$   
399 in PSNR/SAM/ERGAS/SSIM. In terms of visual assessments  
400 (see Fig. 5), we present the pseudo-color representations of  
401 the fused products and some error maps to aid the visual  
402 inspection. Compared to the benchmark, our approach has bet-  
403 ter details and visual effects. Having a look at the error maps,  
404 the reconstruction of BDT is closest to the all zero map, and  
405 significantly lower values than compared approaches.

406 **Results on Harvard Dataset:** Besides, we evaluate the per-  
407 formance of our BDT on another hyperspectral image dataset  
408 (*i.e.*, Harvard). We consider the original HSI as ground-  
409 truth, and simulate the LR-HSI in the same way as the CAVE  
410 dataset. From Tab. 1, the results show that deep learning ap-  
411 proaches outperform traditional ones. Our method gets the  
412 best results (outperforms high-performance approaches such  
413 as DHIF and Fusformer). The proposed approach shows an  
414 excellent trade-off between performance and computational  
415 costs on the Harvard dataset.

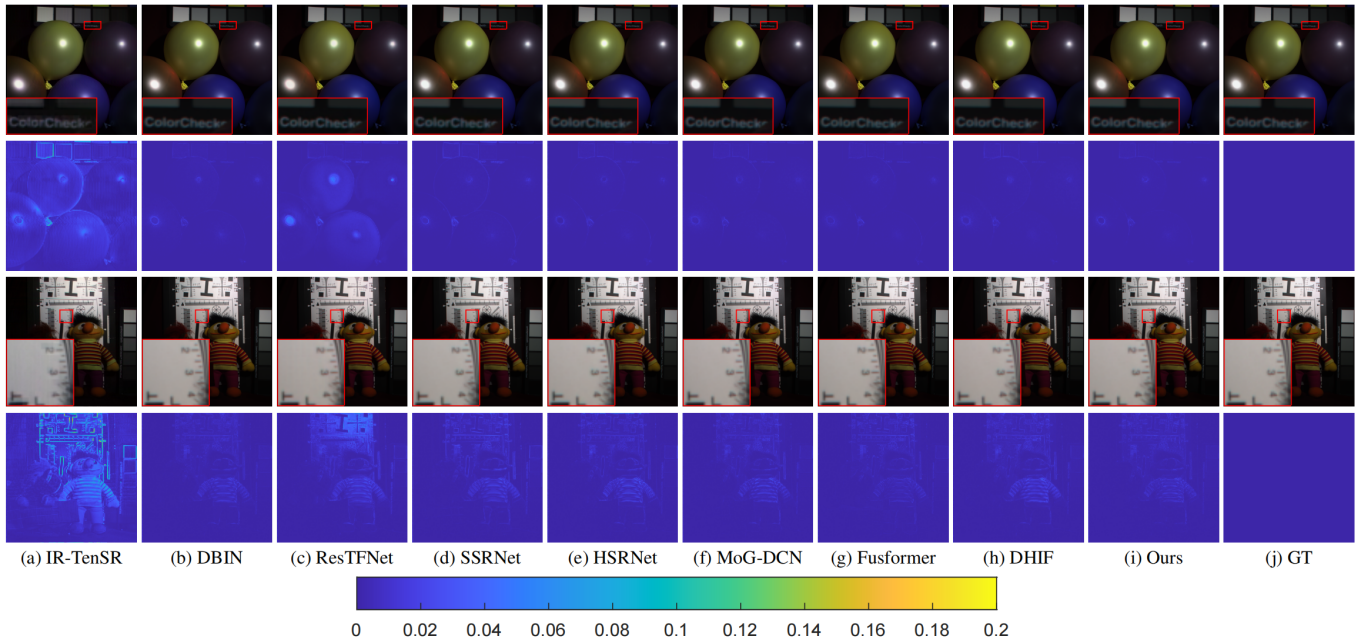


Figure 5: The first and third rows show the results using the pseudo-color representation on “balloons” and “chart and stuffed toy”, respectively, from the CAVE dataset. Some close-ups are depicted in the red rectangles. The second and fourth rows show the residuals between the GT and the fused products. (a) IR-TenSR [Xu *et al.*, 2022], (b) DBIN [Wang *et al.*, 2019], (c) ResTFNet [Liu *et al.*, 2020], (d) SSRNet [Zhang *et al.*, 2020], (e) HSRNet [Hu *et al.*, 2021], (f) MoG-DCN [Dong *et al.*, 2021], (g) Fusformer [Hu *et al.*, 2022], (h) DHIF [Huang *et al.*, 2022], (i) Ours, and (j) GT.

(Restormer-G). After using the proposed D-Spa and G-Spe, the performance of Swin Transformer and Restormer have corresponding enhancement in Tab. 3. It proves that the proposed D-Spa and G-Spe improve the network performance for solving the MHIF task.

3) *Spatial grouped design in G-Spe*: In the Tab. 4, we tested the performance of Spe-MSA and G-Spe without spectral multi-head (w/o head), using BFE in BDT as the backbone. Specifically, the Spe-MSA structure is grouped in the spectral dimension, and the G-Spe structure is grouped in the spatial dimension. The result shows that the effect of the spatial grouped design outperforms slightly than spectral dimension on the MHIF task.

Table 4: The average four QIs and the corresponding parameters on the CAVE dataset simulating a scaling factor of 4. w/o head means G-Spe without spectral multi-head. G means gillions.

Methods	PSNR	SAM	ERGAS	SSIM	#Flops
Spe-MSA	$52.03 \pm 3.79$	$2.02 \pm 0.59$	$1.04 \pm 0.75$	$0.997 \pm 0.0014$	33.52G
w/o head	<b><math>52.09 \pm 3.78</math></b>	<b><math>2.00 \pm 0.58</math></b>	<b><math>1.03 \pm 0.75</math></b>	<b><math>0.997 \pm 0.0013</math></b>	33.87G

4) *D-Spa with different dilations*: We investigated the impact of different dilation rates on the MHIF task by designing D-Spa. The proposed D-Spa has adjustable dilations that can expand and hollow the window in Fig.3, thereby increasing the receptive field. As shown in Tab.5, we found that a dilation rate of 2 yields the best results among the choices of 1, 2, and 3. Thus, D-Spa can provide a long-range response from a flexible range, and it outperforms Spa-MSA in terms of achieving better results.

5) *Test of multi-scaled input in bidirectional branch*: We

Table 5: The average four QIs and the corresponding parameters on the CAVE dataset simulating a scaling factor of 4.  $d$  indicates the dilation rate in D-Spa.

Method	PSNR	SAM	ERGAS	SSIM
$d = 1$	$52.03 \pm 3.79$	$2.02 \pm 0.59$	$1.04 \pm 0.75$	$0.997 \pm 0.0014$
$d = 2$	<b><math>52.30 \pm 3.98</math></b>	<b><math>1.93 \pm 0.55</math></b>	<b><math>1.02 \pm 0.77</math></b>	<b><math>0.997 \pm 0.0014</math></b>
$d = 3$	$51.51 \pm 3.91$	$2.18 \pm 0.65$	$1.11 \pm 0.83$	$0.997 \pm 0.0019$

gradually reduced the participation of the spectral branch in the BFF process. The results in Tab. 6 show the spectral branch plays a vital role in the restoration of image details.

Table 6: The four average QIs and the corresponding parameters on the 11 testing images from the CAVE dataset simulating a scaling factor of 4.  $\mathcal{G}_1$ ,  $\mathcal{G}_2$ , and  $\mathcal{G}_3$  indicate the output which is the result of G-Spe in spectral branch. G refers gillions.

$\mathcal{G}_1$	$\mathcal{G}_2$	$\mathcal{G}_3$	PSNR	SAM	ERGAS	SSIM	#Flops
✓	✓	✓	<b><math>52.30 \pm 3.98</math></b>	<b><math>1.93 \pm 0.55</math></b>	<b><math>1.02 \pm 0.77</math></b>	<b><math>0.997 \pm 0.0014</math></b>	33.52G
✗	✓	✓	$52.04 \pm 3.84$	$1.99 \pm 0.57$	$1.03 \pm 0.76$	$0.997 \pm 0.0014$	33.44G
✗	✗	✓	$51.91 \pm 3.70$	$2.02 \pm 0.59$	$1.03 \pm 0.73$	$0.997 \pm 0.0012$	<b><math>33.10G</math></b>
✗	✗	✗	$50.72 \pm 3.48$	$4.48 \pm 1.38$	$3.84 \pm 1.15$	$0.993 \pm 0.0013$	<b><math>27.74G</math></b>

## 5 Conclusions

This paper proposes the BDT, a Transformer fusion framework, to address the MHIF problem, which employs D-Spa, G-Spe, and bidirectional modules. Specifically, motivated by the MHIF problem, D-Spa and G-Spe are used for spatial and spectral information extraction, respectively.

## References

- [Bandara and Patel, 2022] Wele Gedara Chaminda Bandara and Vishal M Patel. Hypertransformer: A textural and spectral feature fusion transformer for pansharpening. In *CVPR*, pages 1767–1777, 2022.
- [Cao *et al.*, 2020] Xiangyong Cao, Jing Yao, Zongben Xu, and Deyu Meng. Hyperspectral image classification with convolutional neural network and active learning. *IEEE Trans. Geosci. Remote Sens.*, 58(7):4604–4616, 2020.
- [Dian and Li, 2019] Renwei Dian and Shutao Li. Hyperspectral image super-resolution via subspace-based low tensor multi-rank regularization. *IEEE Trans. Image Process.*, 28(10):5135–5146, 2019.
- [Dian *et al.*, 2019] Renwei Dian, Shutao Li, and Leyuan Fang. Learning a low tensor-train rank representation for hyperspectral image super-resolution. *IEEE Trans. Neural Netw. Learn. Syst.*, 30(9):2672–2683, 2019.
- [Dong *et al.*, 2021] Weisheng Dong, Chen Zhou, Fangfang Wu, Jinjian Wu, Guangming Shi, and Xin Li. Model-guided deep hyperspectral image super-resolution. *IEEE Trans. Image Process.*, 30:5754–5768, 2021.
- [Feng and Sun, 2012] Yaoze Feng and Dawen Sun. Application of hyperspectral imaging in food safety inspection and control: a review. *Crit. Rev. Food Sci. Nutr.*, 52(11):1039–1058, 2012.
- [Gao *et al.*, 2006] Bocai Gao, C Davis, and A Goetz. A review of atmospheric correction techniques for hyperspectral remote sensing of land surfaces and ocean color. In *IEEE International Symposium on Geoscience and Remote Sensing*, pages 1979–1981. IEEE, 2006.
- [Gardner and Dorling, 1998] Matt W Gardner and SR Dorling. Artificial neural networks (the multilayer perceptron)—a review of applications in the atmospheric sciences. *Atmos. Environ.*, 32(14-15):2627–2636, 1998.
- [Guo *et al.*, 2020] Penghao Guo, Peixian Zhuang, and Yecai Guo. Bayesian pan-sharpening with multiorder gradient-based deep network constraints. *IEEE J. Sel. Top. Appl. Earth Obs. Remote Sens.*, 13:950–962, 2020.
- [Han *et al.*, 2021] Qi Han, Zejia Fan, Qi Dai, Lei Sun, Ming-Ming Cheng, Jiaying Liu, and Jingdong Wang. On the connection between local attention and dynamic depth-wise convolution. In *ICLR*, 2021.
- [Hong *et al.*, 2021] Danfeng Hong, Zhu Han, Jing Yao, Lianru Gao, Bing Zhang, Antonio Plaza, and Jocelyn Chanussot. Spectralformer: Rethinking hyperspectral image classification with transformers. *IEEE Trans. Geosci. Remote Sens.*, 60:1–15, 2021.
- [Hu *et al.*, 2018] Jie Hu, Li Shen, and Gang Sun. Squeeze-and-excitation networks. In *CVPR*, June 2018.
- [Hu *et al.*, 2021] Jinfan Hu, Tingzhu Huang, Liangjian Deng, Taixiang Jiang, Gemine Vivone, and Jocelyn Chanussot. Hyperspectral image super-resolution via deep spatio-spectral attention convolutional neural networks. *IEEE Trans. Neural Netw. Learn. Syst.*, 2021.
- [Hu *et al.*, 2022] Jinfan Hu, Tingzhu Huang, Liangjian Deng, Hongxia Dou, Danfeng Hong, and Gemine Vivone. Fusformer: A transformer-based fusion network for hyperspectral image super-resolution. *IEEE Geosci. Remote Sens. Lett.*, 19:1–5, 2022.
- [Huang *et al.*, 2022] Tao Huang, Weisheng Dong, Jinjian Wu, Leida Li, Xin Li, and Guangming Shi. Deep hyperspectral image fusion network with iterative spatio-spectral regularization. *IEEE Trans. Comput Imaging.*, 8:201–214, 2022.
- [Jiao *et al.*, 2023] Jiayu Jiao, Yu-Ming Tang, Kun-Yu Lin, Yipeng Gao, Jinhua Ma, Yaowei Wang, and Wei-Shi Zheng. Dilateformer: Multi-scale dilated transformer for visual recognition. *IEEE Transactions on Multimedia*, pages 1–14, 2023.
- [Kolesnikov *et al.*, 2021] Alexander Kolesnikov, Alexey Dosovitskiy, Dirk Weissenborn, Georg Heigold, Jakob Uszkoreit, Lucas Beyer, Matthias Minderer, Mostafa Dehghani, Neil Houlsby, Sylvain Gelly, Thomas Unterthiner, and Xiaohua Zhai. An image is worth 16x16 words: Transformers for image recognition at scale. *ICLR*, 2021.
- [Li *et al.*, 2018a] Shutao Li, Renwei Dian, Leyuan Fang, and José M Bioucas-Dias. Fusing hyperspectral and multispectral images via coupled sparse tensor factorization. *IEEE Trans. Image Process.*, 27(8):4118–4130, 2018.
- [Li *et al.*, 2018b] Yuhong Li, Xiaofan Zhang, and Deming Chen. Csrnet: Dilated convolutional neural networks for understanding the highly congested scenes. In *CVPR*, pages 1091–1100, 2018.
- [Li *et al.*, 2021] Duo Li, Jie Hu, Changhu Wang, Xiangtai Li, Qi She, Lei Zhu, Tong Zhang, and Qifeng Chen. Involution: Inverting the inherence of convolution for visual recognition. In *CVPR*, pages 12321–12330, 2021.
- [Liang *et al.*, 2021] Jingyun Liang, Jie Zhang Cao, Guolei Sun, Kai Zhang, Luc Van Gool, and Radu Timofte. Swinir: Image restoration using swin transformer. In *ICCV*, pages 1833–1844, 2021.
- [Liu *et al.*, 2020] Xiangyu Liu, Qingjie Liu, and Yunhong Wang. Remote sensing image fusion based on two-stream fusion network. *Inf. Fusion.*, 55:1–15, 2020.
- [Liu *et al.*, 2021] Ze Liu, Yutong Lin, Yue Cao, Han Hu, Yixuan Wei, Zheng Zhang, Stephen Lin, and Baining Guo. Swin transformer: Hierarchical vision transformer using shifted windows. In *ICCV*, pages 10012–10022, 2021.
- [Lu *et al.*, 2020] Bing Lu, Phuong D Dao, Jianguo Liu, Yuhong He, and Jiali Shang. Recent advances of hyperspectral imaging technology and applications in agriculture. *Remote Sens. (Basel)*, 12(16):2659, 2020.
- [Ma *et al.*, 2021] Qing Ma, Junjun Jiang, Xianming Liu, and Jiayi Ma. Learning a 3d-cnn and transformer prior for hyperspectral image super-resolution. *arXiv preprint arXiv:2111.13923*, 2021.
- [Meng *et al.*, 2022] Xiangchao Meng, Nan Wang, Feng Shao, and Shutao Li. Vision transformer for pansharpening. *IEEE Trans. Geosci. Remote Sens.*, 60:1–11, 2022.



- 580 [Piqueras *et al.*, 2011] S Piqueras, L Duponchel, R Tauler, 634  
581 and A De Juan. Resolution and segmentation of 635  
582 hyperspectral biomedical images by multivariate curve 636  
583 resolution-alternating least squares. *Anal. Chim. Acta.*, 637  
584 705(1-2):182–192, 2011.
- 585 [Selva *et al.*, 2015] Massimo Selva, Bruno Aiazzi,  
586 Francesco Butera, Leandro Chiarantini, and Stefano  
587 Baronti. Hyper-sharpening: A first approach on sim-ga  
588 data. *IEEE J. Sel. Top Appl. Earth Obs. Remote Sens.*,  
589 8(6):3008–3024, 2015.
- 590 [Wang *et al.*, 2019] Wu Wang, Weihong Zeng, Yue Huang,  
591 Xinghao Ding, and John Paisley. Deep blind hyperspectral  
592 image fusion. In *ICCV*, October 2019.
- 593 [Wang *et al.*, 2020] Sinong Wang, Belinda Z Li, Madian  
594 Khabsa, Han Fang, and Hao Ma. Linformer: Self-attention  
595 with linear complexity. *arXiv preprint arXiv:2006.04768*,  
596 2020.
- 597 [Wu *et al.*, 2011] Jian Wu, Dao-Li Peng, et al. Advances  
598 in researches on hyperspectral remote sensing forestry  
599 information-extracting technology. *Spectrosc. Spect.*  
600 *Anal.*, 31(9):2305–2312, 2011.
- 601 [Xu *et al.*, 2022] Ting Xu, Tingzhu Huang, Liangjian Deng,  
602 and Naoto Yokoya. An iterative regularization method  
603 based on tensor subspace representation for hyperspec-  
604 tral image super-resolution. *IEEE Trans. Geosci. Remote*  
605 *Sens.*, 60:1–16, 2022.
- 606 [Yan *et al.*, 2022] Keyu Yan, Man Zhou, Jie Huang, Feng  
607 Zhao, Chengjun Xie, Chongyi Li, and Danfeng Hong.  
608 Panchromatic and multispectral image fusion via alternat-  
609 ing reverse filtering network. *NeurIPS*, 2022.
- 610 [Yang *et al.*, 2020a] Yong Yang, Chenxu Wan, Shuying  
611 Huang, Hangyuan Lu, and Weiguo Wan. Pansharpening  
612 based on low-rank fuzzy fusion and detail supplement.  
613 *IEEE J. Sel. Top Appl. Earth Obs. Remote Sens.*, 13:5466–  
614 5479, 2020.
- 615 [Yang *et al.*, 2020b] Yong Yang, Lei Wu, Shuying Huang,  
616 Weiguo Wan, Wei Tu, and Hangyuan Lu. Multiband  
617 remote sensing image pansharpening based on dual-  
618 injection model. *IEEE J. Sel. Top Appl. Earth Obs. Re-*  
619 *mote Sens.*, 13:1888–1904, 2020.
- 620 [Zamir *et al.*, 2022] Syed Waqas Zamir, Aditya Arora,  
621 Salman Khan, Munawar Hayat, Fahad Shahbaz Khan, and  
622 Mingsuan Yang. Restormer: Efficient transformer for  
623 high-resolution image restoration. In *CVPR*, pages 5728–  
624 5739, 2022.
- 625 [Zhang *et al.*, 2020] Xueting Zhang, Wei Huang, Qi Wang,  
626 and Xuelong Li. Ssr-net: Spatial-spectral reconstruc-  
627 tion network for hyperspectral and multispectral image  
628 fusion. *IEEE Trans. Geosci. Remote Sens.*, 59(7):5953–  
629 5965, 2020.
- 630 [Zhou *et al.*, 2021] Man Zhou, Xueyang Fu, Jie Huang, Feng  
631 Zhao, Aiping Liu, and Rujing Wang. Effective pan-  
632 sharpening with transformer and invertible neural network.  
633 *IEEE Trans. Geosci. Remote Sens.*, 60, 2021.
- [Zhou *et al.*, 2022] Man Zhou, Jie Huang, Keyu Yan, Hu Yu, Xueyang Fu, Aiping Liu, Xian Wei, and Feng Zhao. Spatial-frequency domain information integration for pansharpening. In *ECCV*, pages 274–291. Springer, 2022.